Electronic Supplementary Material (ESI) for Journal of Materials Chemistry A.

Supporting Information

Molybdenum Carbide Nanoparticles Decorated Hierarchical Tubular Carbon Superstructures with Vertical Nanosheet Arrays for Efficient Hydrogen Evolution

Chemicals. Nickel nitrate hexahydrate ($Ni(NO_3)_2 \cdot 6H_2O$), sodium molybdate dihydrate ($Na_2MoO_4 \cdot 2H_2O$), cobalt nitrate hexahydrate ($Co(NO_3)_2 \cdot 6H_2O$), *p*-phenylenediamine (PPD), N-methyl-2-pyrrolidone (NMP), dimethylformamide (DMF), HCl, H_2SO_4 and KOH were purchased from Tansoole Chemical Ltd. Pyromellitic dianhydride (PMDA) were purchased from Aladdin Chemical Ltd. Commercial Mo_2C powder (99.5 %) and Pt/C (20 %) was purchased from Strem Chemicals, Inc. All the reagents were of analytical grade and used as received without further purification.

Preparation of $NiMoO_4$ Nanorods. $NiMoO_4$ nanorods were fabricated by a previously reported method with modification.[S1] Typically, $Ni(NO_3)_2 \cdot 6H_2O$ (10 mmol) and $Na_2MoO_4 \cdot 2H_2O$ (10 mmol) were firstly dissolved in water (300 mL) and the resulting solution was thermally treated at 160 ^oC for 6 h in a Teflon-lined autoclave. After naturally cooling down to room temperature, $NiMoO_4$ nanorods (1.67 g, yield ≈ 76%) were collected as the yellow-green powders by filtration, washing with water and ethanol, and vacuum drying overnight.

Preparation of PAA and $NiMoO_4$/PIs. PPD (1.041 g) and PMDA (2.121 g) were consecutively dissolved in NMP (or DMF, 60 mL) to exert condensation reaction. After stirred at ambient temperature for 12 h, the yellow viscous solution of polyamic acid (PAA) was obtained. Then a certain amount of PAA (10 mL) was diluted with NMP (or DMF, 150 mL) and stirred for 10 min. Subsequently, $NiMoO_4$ (150 mg) was dispersed in NMP (or DMF, 30 mL) under ultrasonication and then mixed with the PAA solution. The in-situ polycondensation reaction of PAA in the presence of $NiMoO_4$ was exerted under refluxing and vigorous stirring at 180 °C for 2h in a 500 mL two-neck round-bottom flask. After cooled down to room temperature, the precipitates were filtered, washed by NMP (or DMF) and ethanol for several times and vacuum dried at 60 °C. According to the solvent used in the synthetic process, the composites are denoted as $NiMoO_4/PI_{NMP}$ and $NiMoO_4/PI_{DMF}$, respectively. To study the time evolution process of $NiMoO_4$/PI hybrids, samples were extracted from the reaction solution at different polymerization time at 180 °C.

Preparation of $CoMoO_4$ Nanorods and $CoMoO_4$/PIs.The synthesis of $CoMoO_4$ nanorods is similar to that of $NiMoO_4$ nanorods except replacing $Ni(NO_3)_2 \cdot 6H_2O$ with $Co(NO_3)_2 \cdot 6H_2O$. The synthesis of $CoMoO_4$/PIs is analogous to that of $NiMoO_4$/PIs by simply replacing $NiMoO_4$ nanorods with $CoMoO_4$ nanorods.

Preparation of Mo_2C/CTSSs. $NiMoO_4$/PI hybrids were heated in a tube furnace under 5% H_2/Ar flow with a ramp rate of 5 °C min^{-1}, maintained at 800 °C for 5 h and then cooled down naturally. The samples were then treated with 3M HCl aqueous solution at 80 °C for 12 h to remove unstable and inactive species. After filtration, washing and drying, the samples, denoted as Mo_2C/CTSS, were collected for future use. Based on the arrangement of nanosheet arrays, the resulting product was denoted as Mo_2C/CTSS-P (Periodic, from $NiMoO_4/PI_{NMP}$) and Mo_2C/CTSS-R (Random, from $NiMoO_4/PI_{DMF}$), respectively.

Structural Characterization. Fourier transform infrared spectroscopy (FTIR) spectra were surveyed using Spectrum 100 (Pekin Elmer, Inc., USA) spectrometer with the KBr pellet technique. X-ray diffraction (XRD) was performed on a Bruker D8 Advance powder diffractometer (X-ray source: Cu, wavelength = 1.5406 Å). Scanning electron microscopy

(SEM) images were obtained on a FEI Nova scanning electron microscope at an electric voltage of 5 KV. Transmission electron microscopy (TEM) characterizations were conducted using a JEM-2100 (JEOL Ltd., Japan) with an accelerating voltage of 200 KV, samples were dispersed in ethanol with sonication and then dropped onto Cu grids for observation. Elemental mapping images were recorded using EDX spectroscope attached to the TEM. The Brunauer–Emment–Teller (BET) specific surface areas of the samples were calculated by the N_2 adsorption isothermal curves from an ASAP 2010 M/C surface area and porosimetry analyzer (Micromeritics Instrument Corporation, USA). X-ray photoelectron spectroscopy (XPS) experiments were carried out on a AXIS Ultra DLD system from Kratos with Al Kα radiation as X-ray source for radiation. Thermal gravimetric analysis (TGA) of the samples was measured by using a TA-Instruments Q5000IR thermo gravimetric analyzer in nitrogen flow (100 mL min^{-1}) or air atmosphere with a temperature increasing rate of 10 ^{o}C min^{-1}. The elemental content of Ni in the Mo_2C/CTSSs were analyzed by inductively coupled plasma spectroscopy (ICP, iCAP7600).

Electrocatalytic Measurements. The hydrogen evolution reaction (HER) performance of the samples was studied with a standard three-electrode system using a CHI 660e electrochemical station (Shanghai Chenhua Co., China) at room temperature. An Ag/AgCl (3 M KCl) electrode and a Pt wire electrode were used as reference electrode and counter electrode, respectively. To prepare the working electrode, the sample (5 mg) was first dispersed in the ethanol solution of Nafion (0.5 wt%, 500 μL), and then was sonicated for at least 1h to achieve a homogeneous ink. Subsequently, the catalyst ink (9 μL) was pipetted onto a glassy carbon electrode (d=5.61 mm, S=0.2472 cm^2) with a loading of 0.75

mg/cm^2. The electrochemical experiments were conducted in N_2 saturated acidic (0.5 M H_2SO_4) or alkaline (1 M KOH) or neutral (0.5 M phosphate buffered saline, PBS) electrolyte. To obtain the polarization curve, linear sweep voltammetry (LSV) was recorded at a scan rate of 5 mV s^{-1}. The Tafel plot is fitted to the Tafel equation (η = b log I + a, where η is the overpotential, I is the current density, b is the Tafel slope and a is the Tafel parameter). The exchange current density of the catalysts is obtained by extrapolating the Tafel plots to zero overpotential. The current-time (*i*-t) chronoamperometric response of $Mo_2C/CTSS_{NMP}$ were tested at an overpotential of 108 mV vs. RHE in 0.5M H_2SO_4 or 110 mV vs. RHE in 1M KOH. The electrochemical impedance spectroscopy (EIS) of samples were tested in both acidic and alkaline solutions at an overpotential of 100 mV. All the electrochemical data were iR-corrected.

The electrochemical active surface areas (ECSAs) of the catalysts were obtained according to the double-layer capacitance (C_{dl}) calculated from their cyclic voltammogram (CV) curves. The CV curves were scaned from 10 to 200 mV s^{-1} in the range from 0.10 to 0.20 V vs RHE. The capacitive currents of ΔJ ($J_{anodic} - J_{cathodic}$) are plotted as a function of the scan rate. The slope of the fitting line is equal to $2C_{dl}$. The following formula was used to calculate the ECSA:

$$\mathrm{ECSA} = C_{dl}/C_s$$

For a flat surface, the specific capacitance (C_s) is generally in the range of 20 ~ 60 μF cm^{-2}. Therefore, 40 μF cm^{-2} was used here for the calculation of ECSA.

The calibration of Ag/AgCl electrode was performed in a standard three-electrode system with Pt wires as the working and counter electrodes, and the Ag/AgCl electrode as the reference electrode. Electrolytes are pre-purged and saturated with high purity H_2. Linear scanning voltammetry (LSV) is then run at a scan rate of 0.1 mV s^{-1}, and the potential at which the current crossed zero is taken to be the thermodynamic potential (vs. Ag/AgCl) for the hydrogen electrode reactions. In 1 M KOH, E (RHE) = E (Ag/AgCl) + 1.026 V. In 0.5M H_2SO_4, E (RHE) = E (Ag/AgCl) + 0.214 V. In 0.5 M PBS, E(RHE)= E (Ag/AgCl) + 0.652 V.

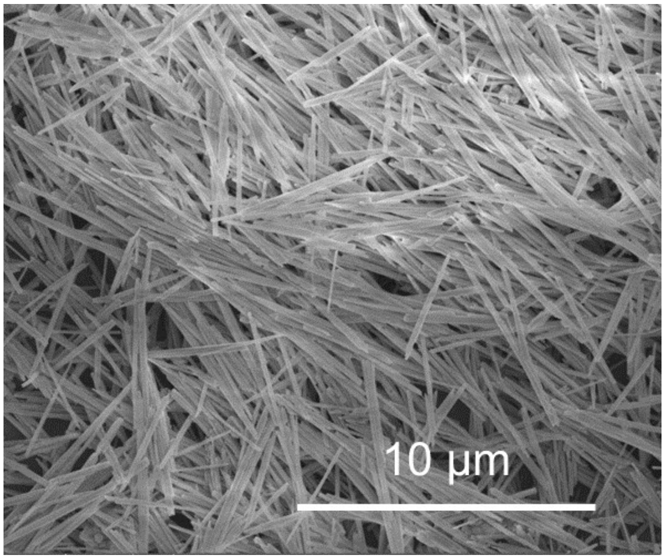

Figure S1. SEM image of $NiMoO_4$ nanorods.

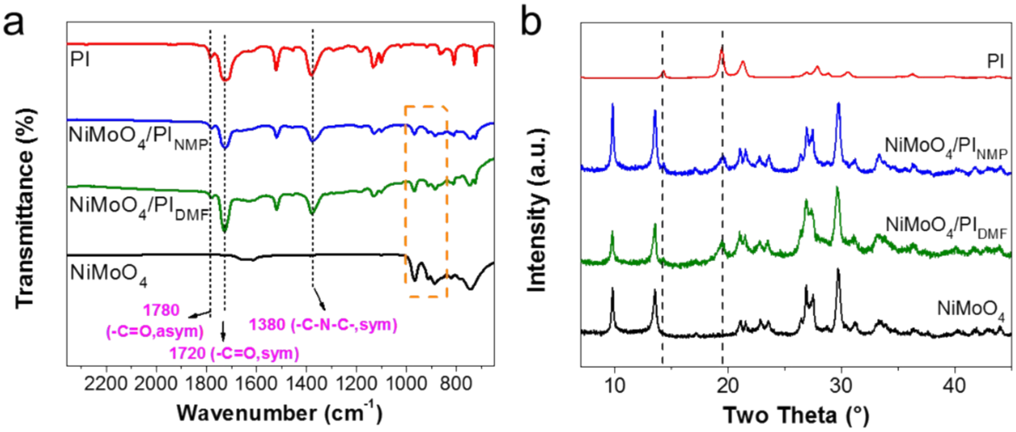

Figure S2. a) FTIR spectra and b) XRD patterns of PI, $NiMoO_4$, $NiMoO_4/PI_{NMP}$, and $NiMoO_4/PI_{DMF}$. As shown in FTIR spectra, the characteristic peaks of PI (1780, 1720, and 1380 cm^{-1}) and $NiMoO_4$ (966, 915, and 889 cm^{-1}) can be found in both $NiMoO_4/PI_{NMP}$ and $NiMoO_4/PI_{DMF}$, confirming the successful synthesis of hybrids. In the XRD patterns of $NiMoO_4$/PIs, the characteristic peaks of PI and $NiMoO_4$ can also be observed, further confirming their successful synthesis.

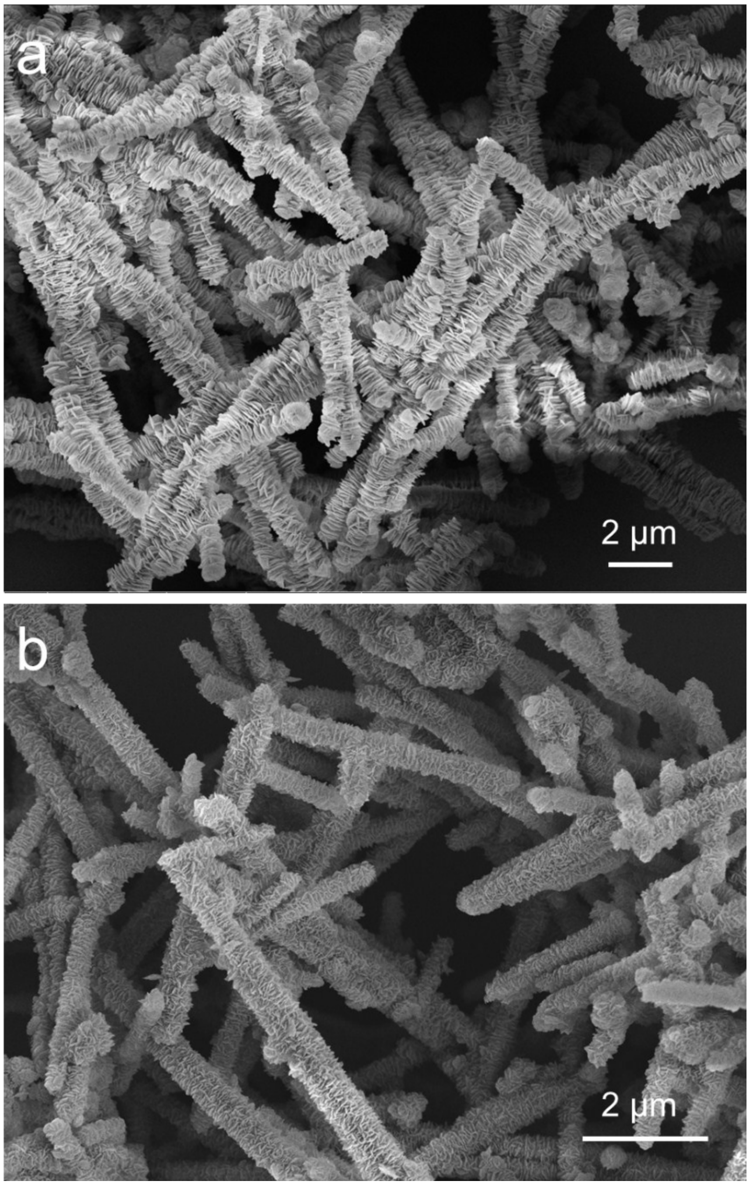

Figure S3. Low-magnified SEM images of a) $NiMoO_4/PI_{NMP}$ and b) $NiMoO_4/PI_{DMF}$.

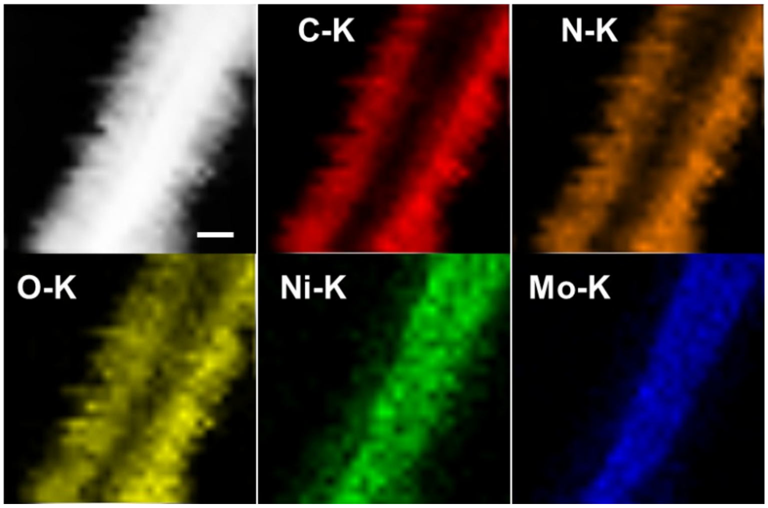

Figure S4. STEM-Mapping images of $NiMoO_4/PI_{NMP}$. The scale bar is 200 nm.

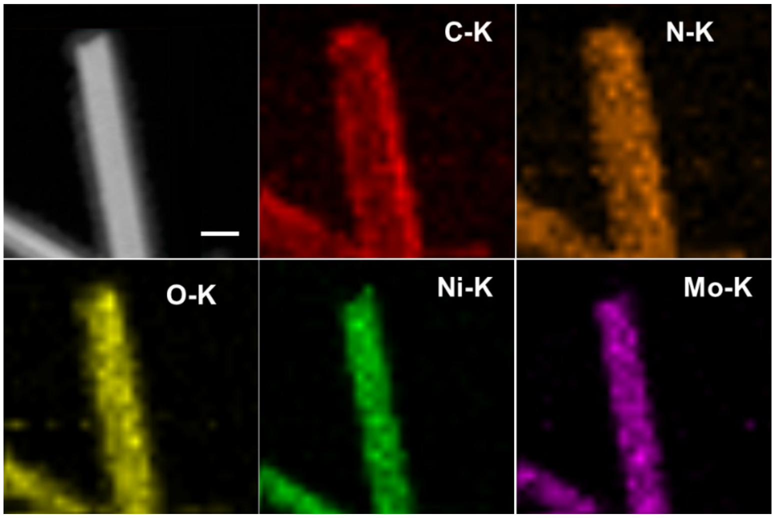

Figure S5. STEM-Mapping images of $NiMoO_4/PI_{DMF}$. The scale bar is 200 nm.

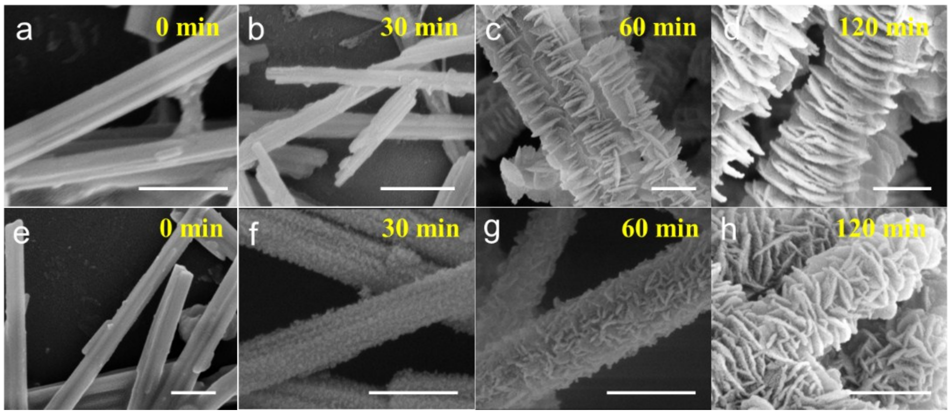

Figure S6. SEM images of a-d) $NiMoO_4/PI_{NMP}$ and e-h) $NiMoO_4/PI_{DMF}$ obtained at differed polymerization time: a, e) 0 min (when the temperature reached 180 ^oC); b, f) 30 min; c, g) 60 min; d, h) 120 min. Scale bars are 500 nm.

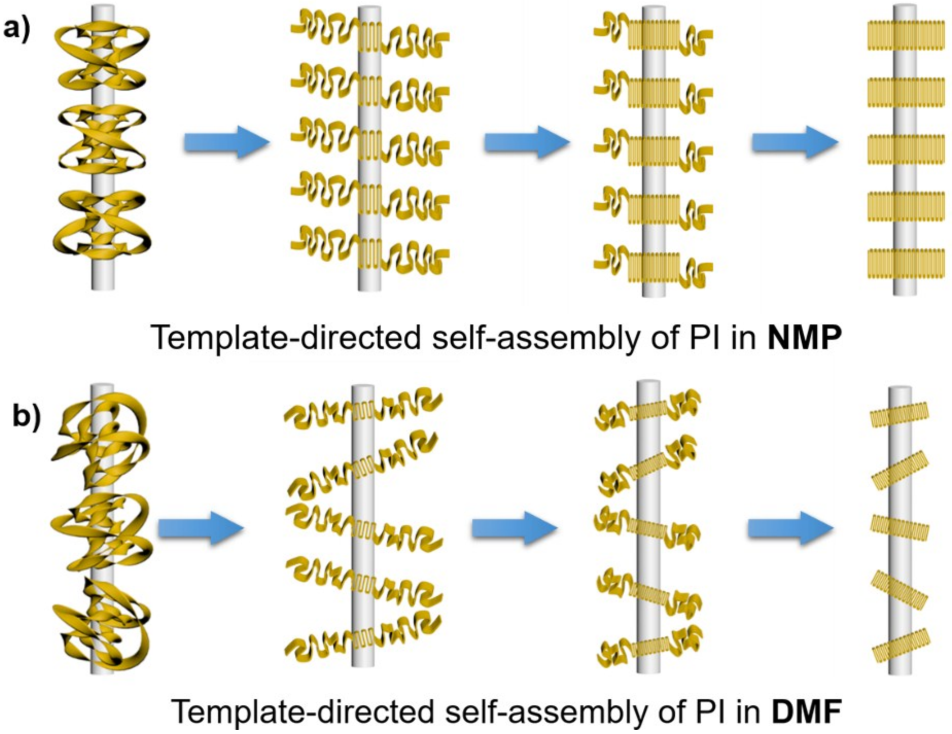

Figure S7. Template-directed self-assembly mechanism for the formation of $NiMoO_4$/PI composites in a) NMP and b) DMF with different arrangement of PI nanosheet arrays.

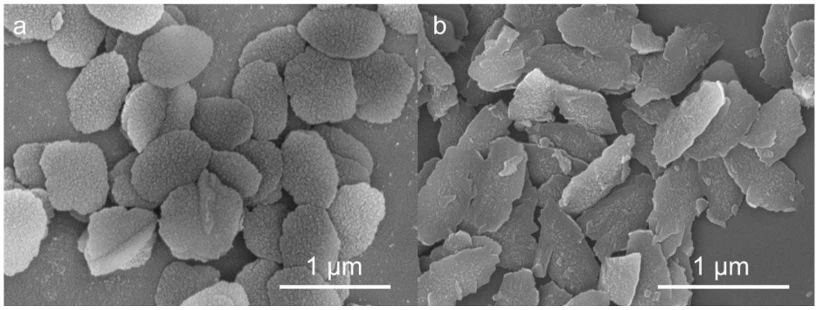

Figure S8. SEM images of PI nanoplates synthesized in a) NMP and b) DMF without the use of $NiMoO_4$ nanorods. The significantly different morphology with/without $NiMoO_4$ reveals the crucial role templates play in the formation of 3D superstructures.

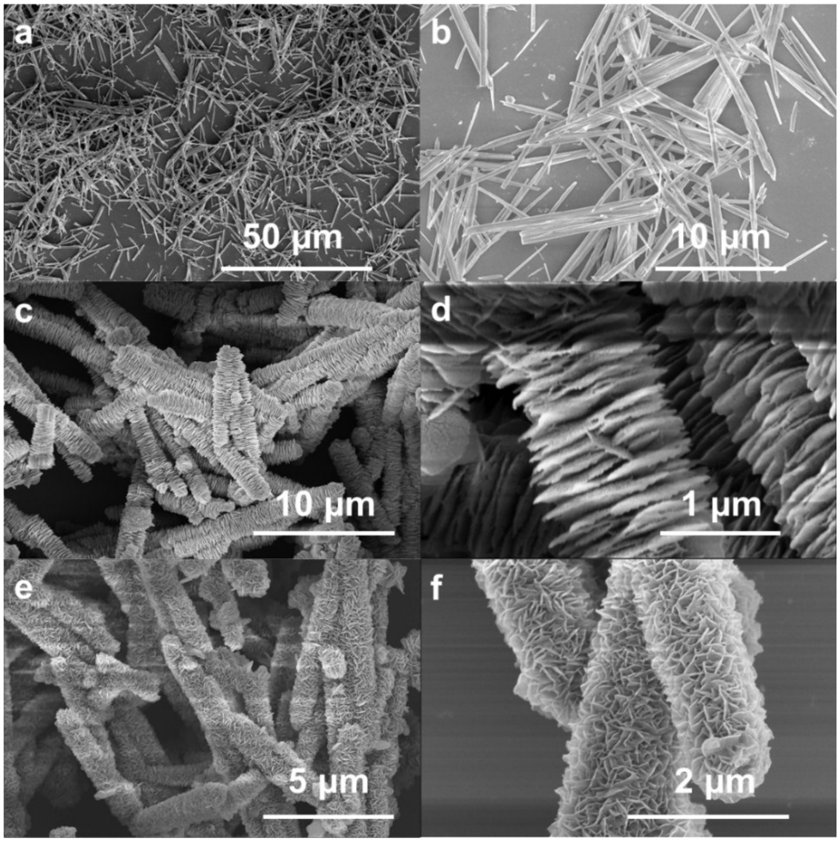

Figure S9. SEM images of (a, b) $CoMoO_4$ nanorods and $CoMoO_4$/PI hybrids synthesized in (c ,d) NMP and (e, f) DMF. The vertically oriented and arrangement-tunable nanosheet arrays can be achieved in the $CoMoO_4$/PI hybrids, i.e, nanosheet arrays with periodic patterns in NMP and random patterns in DMF.

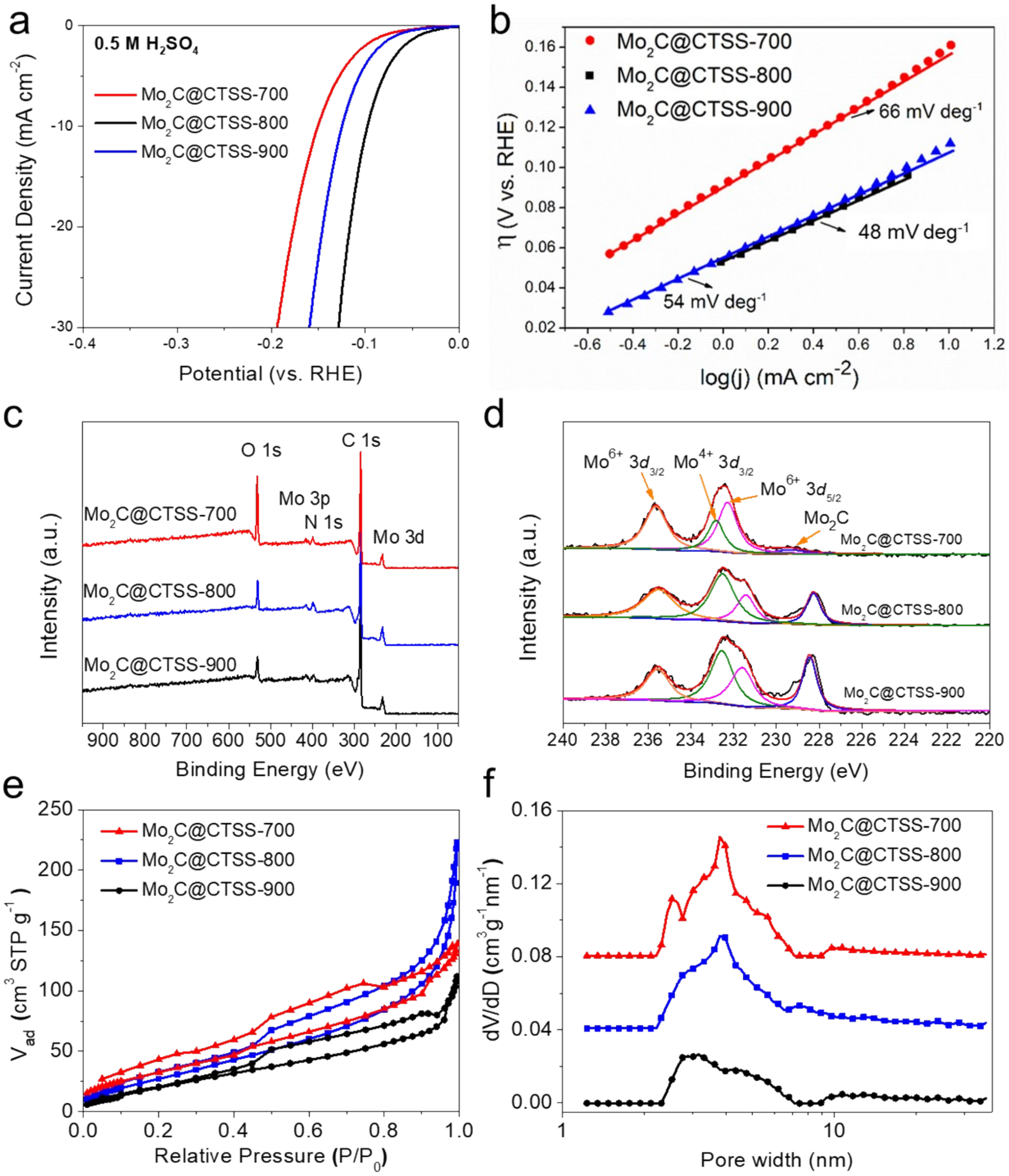

Figure S10. a) Polarization curves and b) Tafel plots of the Mo_2C/CTSS catalysts obtained from different temperatures (700, 800, and 900 °C). c) whole XPS spectra and d) high-resolution Mo 3d curves of Mo_2C/CTSS-700, Mo_2C/CTSS-800, and Mo_2C/CTSS-900. e) N_2 sorption curves and f) corresponding pore size distributions of Mo_2C/CTSSs. To optimize the pyrolysis temperature, three Mo_2C/CTSS based catalysts were synthesized by the thermal treatment of $NiMoO_4$/PI_{NMP} at 700, 800, and 900 °C for 5 h, which were denoted as Mo_2C/CTSS-700, Mo_2C/CTSS-800, and Mo_2C/CTSS-900, respectively. As shown in their polarization curves (Figure S10a), Mo_2C/CTSS-800 only needs an overpotential of 97 mV to deliver a current density of 10 mA cm^{-2}, which is much smaller than those of Mo_2C/CTSS-900 (125 mV) and Mo_2C/CTSS-700 (150 mV). The Tafel slopes of Mo_2C/CTSS-700, Mo_2C/CTSS-800, and Mo_2C/CTSS-900 are calculated as 66, 48, and 54 mV dec^{-1}, respectively (Figure S10b). These results demonstrate that 800 ^{o}C is the optimal temperature for preparing the Mo_2C/CTSS catalysts in this work. As evidenced by the high-resolution Mo 3d spectra, the worst HER performance of Mo_2C/CTSS-700 among the three samples should be due to the incomplete carburization of Mo_2C (the peak at 227~230 eV) in Mo_2C/CTSS-700 (Figure S10c and d). On the other hand, the lower surface area of Mo_2C/CTSS-900 (98 m^2 g^{-1}) than that of Mo_2C/CTSS-800 (117 m^2 g^{-1}) explains its inferior electrocatalytic property (Figure S10e and f).

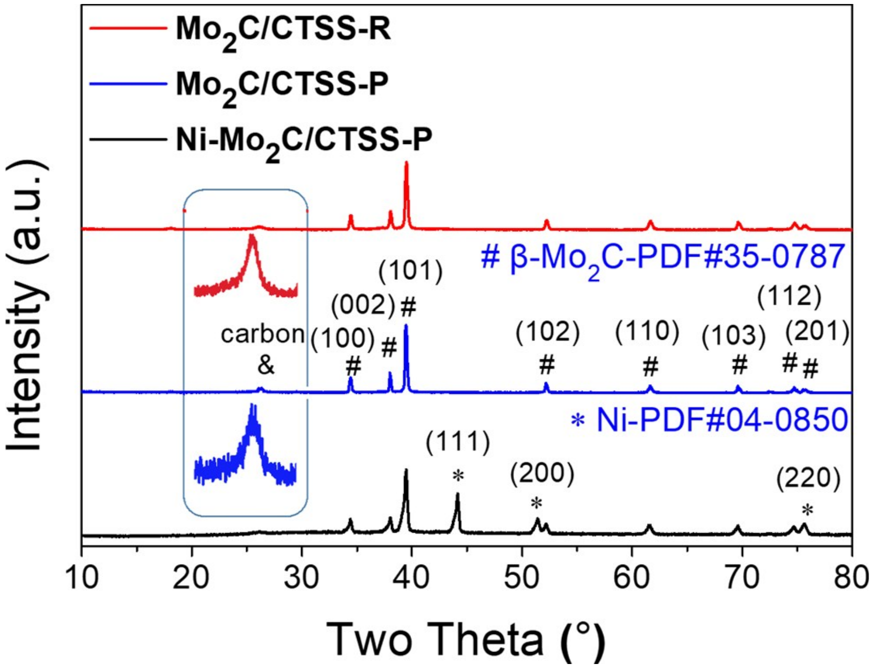

Figure S11. XRD patterns of carbonized $NiMoO_4$/PI before and after etching, Ni-Mo_2C/CTSS-P (black line), Mo_2C/CTSS-P (blue line) and Mo_2C/CTSS-R (red line). Before acidic etching, the diffractions from both Ni and β-Mo_2C can be obtained. After etching, the peaks from metallic Ni disappear and only those corresponding to β-Mo_2C remain. The magnified peak at around 26 °C is attributed to graphitic structure.

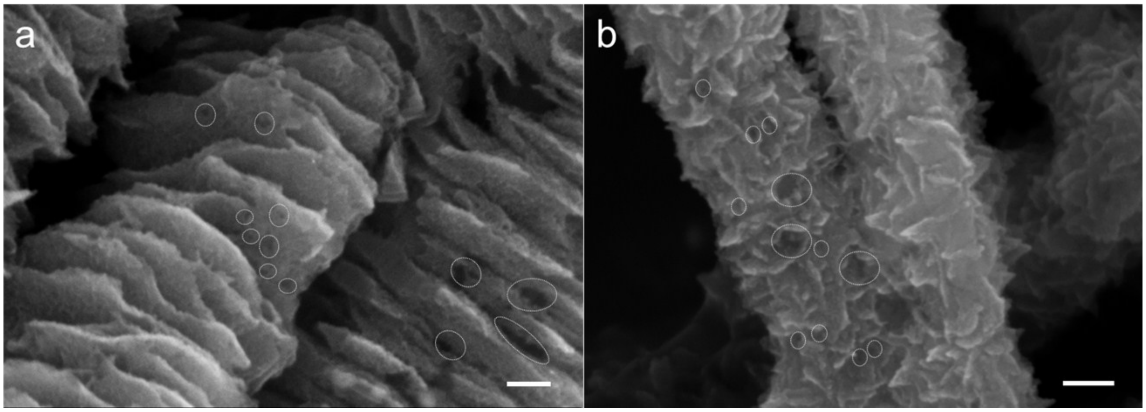

Figure S12. HRTEM images of a) Mo_2C/CTSS-P and b) Mo_2C/CTSS-R. Some easily observed hierarchical pores are cycled out. Scale bars are 100 nm.

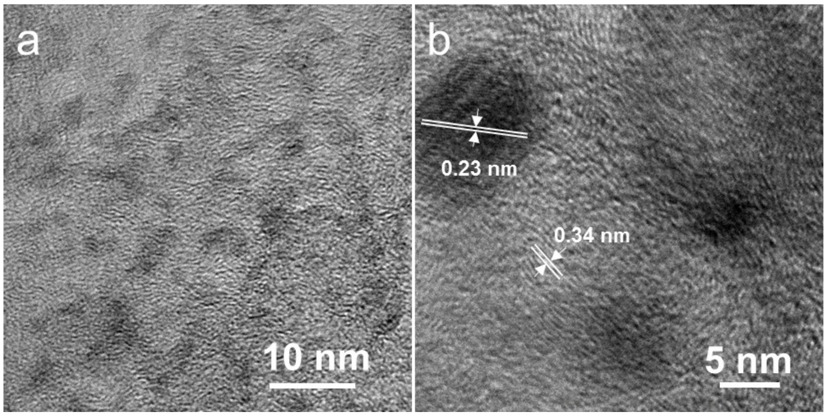

Figure S13. HRTEM images of Mo_2C/CTSS-R indicating the embedment of ultrafine Mo_2C nanoparticles inside the carbon nanosheets with graphitic structure.

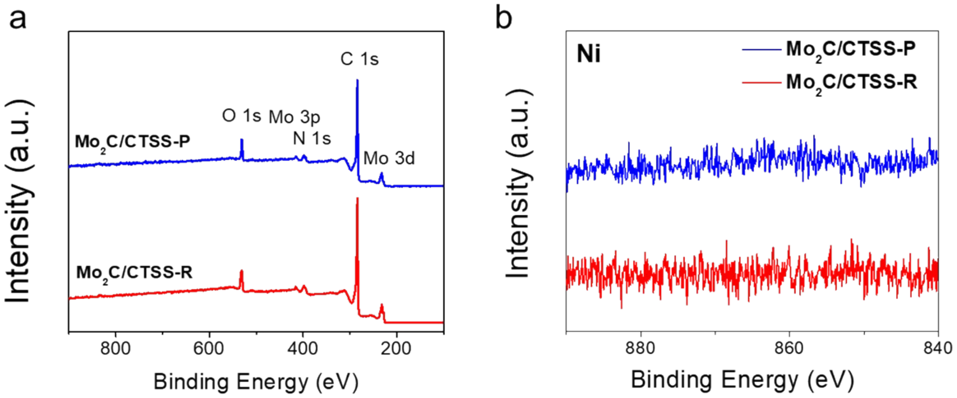

Figure S14. XPS a) whole spectra of Mo_2C/CTSSs indicating the existence of Mo, C, N, O elements in the samples and b) high resolution Ni 1s spectra of Mo_2C/CTSSs revealing no formation of nickel-related chemical bond in the hybrid.

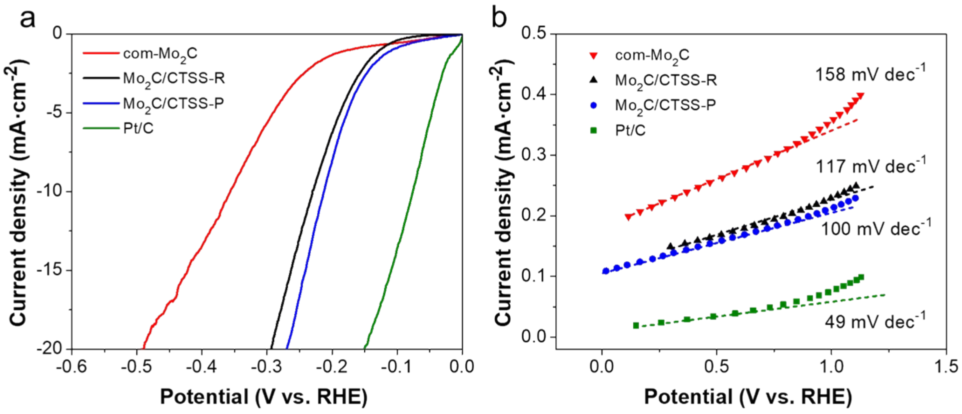

Figure S15. HER performances the of Mo_2C/CTSSs in neutral solution (0.5 M PBS). a) Polarization curves and b) derived Tafel plots of catalysts. According to the polarization curves, to deliver a current density of 10 mA cm^{-2}, Mo_2C/CTSS-P needs the overpotential of 213 mV, superior to Mo_2C/CTSS-R (230 mV) and com-Mo_2C (357 mV), which matches well with the results in alkaline and acidic media. The Tafel slope for Pt/C, Mo_2C/CTSS-P, Mo_2C/CTSS-R, and com-Mo_2C is 49, 100, 117, and 158 mV dec^{-1}, respectively.

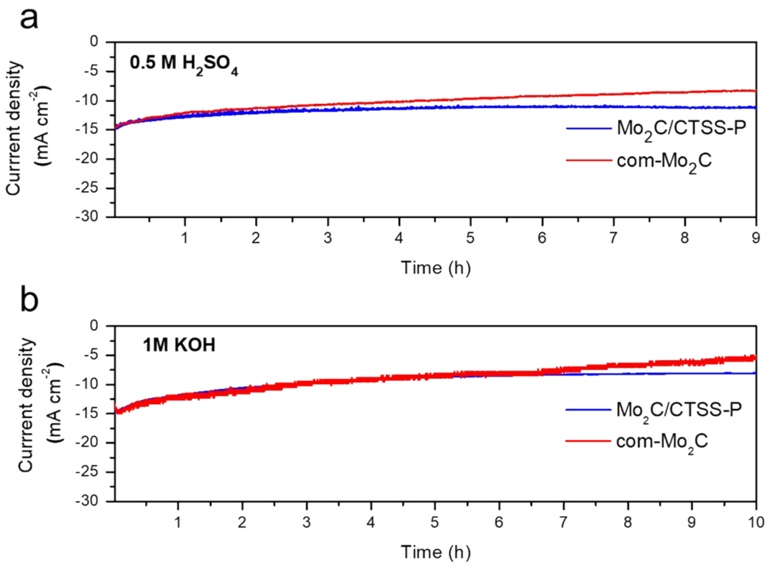

Figure S16. Durability test of Mo_2C with or without the protection of carbon layer. Choronamperometric responses of Mo_2C/CTSS-P and com-Mo_2C in a) 0.5 M H_2SO_4 and b) 1 M KOH.

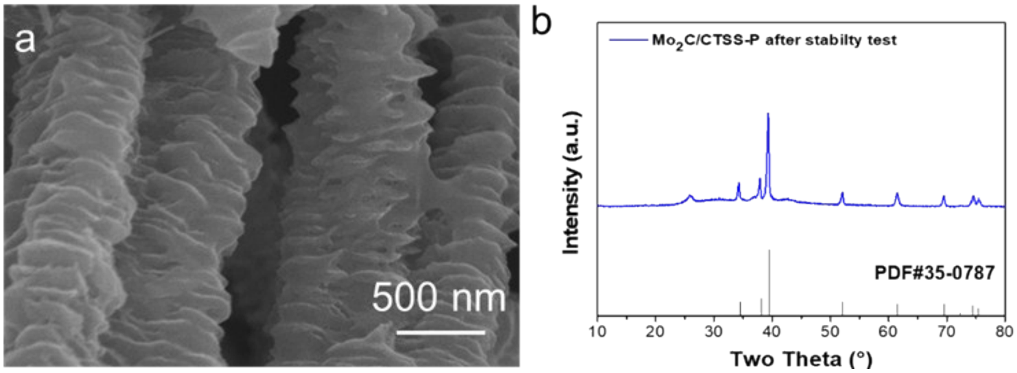

Figure S17. a) SEM image and b) XRD pattern of Mo_2C/CTSS-P after chronoamperometric measurement. The catalyst solution was loaded onto Ni foam for the durability test and then sonicated into ethanol solution after the test for subsequent structural characterization.

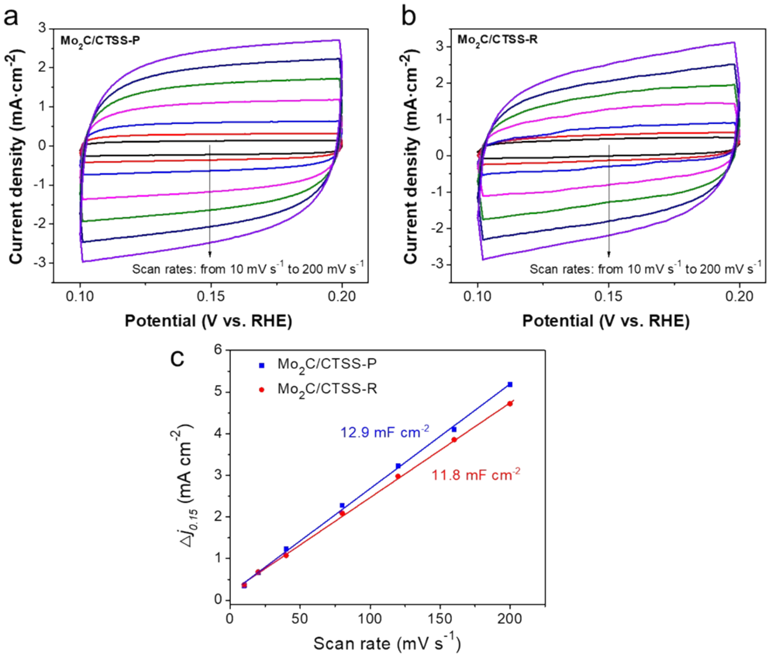

Figure S18. Capacitive current at 0.15 V as a function of scan rates for a) Mo_2C/CTSS-P and b) Mo_2C/CTSS-R in 1 M KOH. c) CV curves at different scan rates from 10 to 200 mV s^{-1}). From the plots, the C_{dl} of Mo_2C/CTSS-P and Mo_2C/CTSS-R is estimated to be 12.9 mF cm^{-2} and 11.8 mF cm^{-2}, respectively. The corresponding ECSA is 322 for Mo_2C/CTSS-P and 295 cm^2 for Mo_2C/CTSS-R.

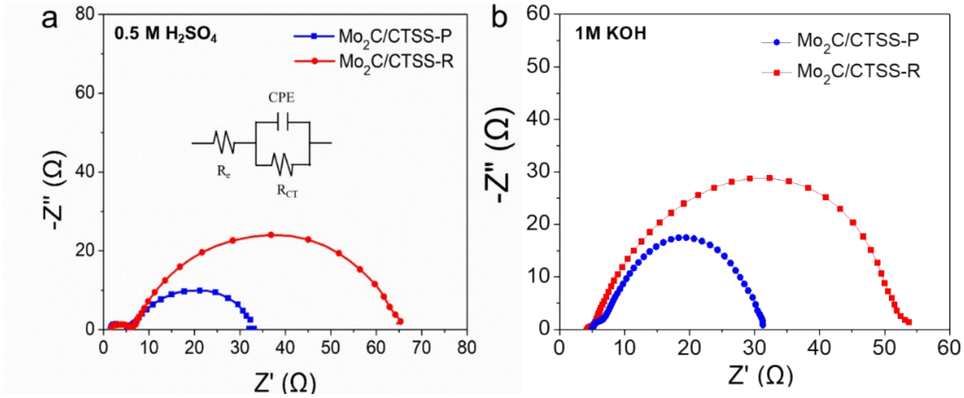

Figure S19. Nyquist plots of Mo_2C/CTSS-P and Mo_2C/CTSS-R on glassy carbon eletrode in a) H_2SO_4 solution (0.5 M) and b) KOH solution (1 M) at an overpotential of 100 mV. Inset shows equivalent circuit used for fitting EIS data. Rs represents the overall series resistance and Rct, the charge transfer resistance. CPE is the constant phase angle element, indicating the double layer capacitance of the electrode in the real-world scenario.

Table S1. Atomic contents of C, N and Mo elements obtained by XPS analysis.

Samples	C content (at. %)	N content (at. %)	Mo content (at. %)
Mo_2C/CTSS-P	89.82	2.71	2.24
Mo_2C/CTSS-R	88.73	2.59	2.32

Table S2. The HER performance of Mo_2C/CTSS in this work and the recently reported Mo_2C catalysts in acidic/alkaline meida.

Materials	Electrolyte	η at 10 mA cm^{-2} (mV vs. RHE)	Tafel slope (mV/dec)	Exchange current density (mA cm^{-2})	Reference
Mo_2C/CTSS-P	0.5 M H_2SO_4	97	48	0.130	This work
	1 M KOH	95	54	0.231	
3DHP-Mo_2C	0.5 M H_2SO_4	166	75	0.287	[S2]
	1 M KOH	139	71	0.441	
MoC_x octahedral	0.5 M H_2SO_4	142	53	0.023	[S3]
	1 M KOH	151	59	0.029	
Mo_2C@NPC/NPRGO	0.5 M H_2SO_4	34	33.6	1.09	[S4]
Mo_2C/C flower	0.5 M H_2SO_4	146	60	0.108	[S5]
P-Mo_2C@C nanowire	0.5 M H_2SO_4	89	42	0.18	[S6]
Mo_2C@2D-NPCs	0.5 M H_2SO_4	86	62	-	[S7]
	1 M KOH	45	46	1.14	
Mo_2C/NCF	0.5 M H_2SO_4	144	55	-	[S8]
	1 M KOH	100	65	-	
Pomegranate-like Mo_2C@C	0.5 M H_2SO_4	141	56	0.029	[S9]
	1 M KOH	47	71	2.042	
Ni/Mo_2C hollow sphere	0.5 M H_2SO_4	192	98	~0.222	[S10]
	1 M KOH	123	84	~0.498	
MoDCA-5	0.5 M H_2SO_4	78	41	0.178	[S11]
Mo_2C	0.5 M H_2SO_4	172	62	0.017	[S12]

nanotubes	0.1 M KOH	112	55	0.087	
Mo_2C@NC	0.5 M H_2SO_4	124	60	0.096	[S13]
	1 M KOH	60	-	-	
PDAP-MoCN-CO_2	0.5 M H_2SO_4	140	46	-	[S14]
Mo_2C/CNT-GR	0.5 M H_2SO_4	130	58	0.062	[S15]
Mo_2C/GCS	0.5 M H_2SO_4	~250	62.6	0.0125	[S16]

References:

[S1] W. Xiao, J. S. Chen, C. M. Li, R. Xu and X. W. Lou, *Chem. Mater.*, **2010**, *22*, 746-754.

[S2] T. Meng, L. Zheng, J. Qin, D. Zhao and M. Cao, *J. Mater. Chem. A*, **2017**, *5*, 20228-20238.

[S3] H. B. Wu, B. Y. Xia, L. Yu, X.-Y. Yu, X. W. Lou, *Nat. Commun.* **2015**, *6*, 6512.

[S4] J. S. Li, Y. Wang, C. H. Liu, S. L. Li, Y. G. Wang, L. Z. Dong, Z. H. Dai, Y. F. Li, Y. Q. Lan, *Nat. Commun.* **2016**, *7*, 11204.

[S5] L. Chen, H. Jiang, H. Jiang, H. Zhang, S. Guo, Y. Hu, C. Li, *Adv. Energy Mater.* **2017**, 1602782.

[S6] Z. Shi, K. Nie, Z.-J. Shao, B. Gao, H. Lin, H. Zhang, B. Liu, Y. Wang, Y. Zhang, X. Sun, X.-M. Cao, P. Hu, Q. Gao, Y. Tang, *Energy Environ. Sci.* **2017**, *10*, 1262.

[S7] C. Lu, D. Tranca, J. Zhang, F. n. Rodríguez Hernández, Y. Su, X. Zhuang, F. Zhang, G. Seifert, X. Feng, *ACS Nano* **2017**, *11*, 3933.

[S8] Y. Huang, Q. Gong, X. Song, K. Feng, K. Nie, F. Zhao, Y. Wang, M. Zeng, J. Zhong, Y. Li, *ACS Nano* **2016**, *10*, 11337.

[S9] Y. Y. Chen, Y. Zhang, W. J. Jiang, X. Zhang, Z. Dai, L. J. Wan, J. S. Hu, *ACS Nano* **2016**, *10*, 8851.

[S10] X. Xu, F. Nosheen, X. Wang, *Chem. Mater.* **2016**, *28*, 6313.

[S11] R. Ma, Y. Zhou, Y. Chen, P. Li, Q. Liu, J. Wang, *Angew. Chem. Int. Ed.* **2015**, *54*, 14723.

[S12] F. X. Ma, H. B. Wu, B. Y. Xia, C. Y. Xu, X. W. Lou, *Angew. Chem. Int. Ed.* **2015**, *54*, 15395.

[S13] Y. Liu, G. Yu, G.-D. Li, Y. Sun, T. Asefa, W. Chen, X. Zou, *Angew. Chem. Int. Ed.* **2015**, *54*, 10752.

[S14] Y. Zhao, K. Kamiya, K. Hashimoto, S. Nakanishi, *J. Am. Chem. Soc.* **2015**, *137*, 110.

[S15] D. H. Youn, S. Han, J. Y. Kim, J. Y. Kim, H. Park, S. H. Choi, J. S. Lee, *ACS Nano* **2014**, *8*, 5164.

[S16] W. Cui, N. Cheng, Q. Liu, C. Ge, A. M. Asiri, X. Sun, *ACS Catal.* **2014**, *4*, 2658.